http://dx.doi.org/10.1016/j.nanoen.2023.108920

Optimizing Cu^{+}-Cu^{0} synergy by *operando* tracking of Cu_2O nanocatalysts during the electrochemical CO_2 reduction reaction

Hao Zhang[a], Ying Wang[b], Qiong Lei[c], Ying Wang[d], Chiu Tang[e], Jun Yin*[c], Tsz Woon Benedict Lo*[a], [c]

a: Department of Applied Biology and Chemical Technology, The Hong Kong Polytechnic University, Hunghom, Hong Kong, China

b: State Key Laboratory of Automotive Simulation and Control, School of Materials Science and Engineering, Key Laboratory of Automobile Materials of MOE, Jilin University, Changchun, 130012 China

c: Department of Applied Physics, The Hong Kong Polytechnic University, Hunghom, Hong Kong, China

d: Department of Chemistry, Chinese University of Hong Kong, Hong Kong, China

e: Diamond Light Source Ltd., Harwell Science and Innovation Campus, Didcot, Oxfordshire, Harwell Campus, Oxford, OX11 0DE, United Kingdom

*Corresponding author.

E-mail address: jun.yin@polyu.edu.hk (Jun Yin), benedict.tw.lo@polyu.edu.hk (Tsz Woon Benedict Lo)

Abstract

Tracking the evolution of electrocatalysts over oxide-derived Cu materials during the electrochemical CO_2 reduction reaction (eCO_2RR) is pivotal for optimizing the product selectivity toward desired multi-carbon (C_{2+}) products. However, the identification of the true intermediate active catalyst is still unclear. Here, we adopted a multi-modal characterization approach, primarily based on operando powder X-ray diffraction and operando micro-Raman spectroscopy, to study three Cu_2O precursors with different morphologies, namely, octahedral (O-), cubic (C-), and nanowire (N-Cu_2O). This multi-modal approach allows us to investigate the Cu_2O nano-crystallites from the interface to the bulk structure. The results suggested notably different electrochemical reduction kinetics. 26.1% O-Cu_2O and 90.6% C-Cu_2O were reduced to much smaller Cu(0) domains after two hours of time-on-stream; N-Cu_2O, with notably higher surface-to-volume ratio, was completely reduced within 45 minutes of time-on-stream. We accordingly observed a structure-reactivity correlation where a more intricate Cu_2O/Cu grain network (and hence Cu^+-Cu^0 junctions) as observed in O-Cu_2O, can lead to stable and quantitative production of ethylene at the Faradic efficiency of around 40% (in stark contrast to those of C- and N-Cu_2O). The synergy between the Cu_2O and Cu phases was also verified by density functional theory calculations. The upshifted d-band center of Cu_2O/Cu in O-Cu_2O is the most conducive toward the production of ethylene, whereas the downshifted d-band center of Cu_2O/Cu in C-Cu_2O leads to a decreased production of ethylene in the expense of unwanted production of hydrogen. We envisage that system optimization and design of new catalysts will become more facile and efficient using a related multi-modal operando characterization philosophy.

1. Introduction

The electrochemical CO_2 reduction reaction (eCO_2RR) has been regarded as an effective approach to mitigating the current CO_2 issues by carbon utilization[1–4]. Oxide-derived Cu (ODC) materials, such as Cu_2O and CuO, are some of the most often studied catalysts that can convert CO_2 into higher multi-carbon feedstock, partly due to the suitable adsorption energy of *CO that further promotes C–C coupling[5–7]. Vast efforts have been made to develop more efficient and selective ODC-based electrocatalysts through surface modifications[8,9], structure engineering[10–12], doping[13] and morphology control[14–17].

When operated under the eCO_2RR conditions (typically –0.8 to –1.1 V vs RHE), ODC materials are prone to electrochemical reduction (giving metallic Cu) as shown in the Pourbaix diagram[18]. Nonetheless, the presence of surface Cu^+ and/or sub-surface oxygen species has been shown influential on the C_2 product selectivity. In the study by Mistry and co-workers, the survival of Cu^+ on the catalyst surface was reported during the eCO_2RR based on spectroscopic findings[19]. Goddard III and co-workers reported the much-promoted kinetics and thermodynamics of both CO_2 activation and CO* coupling from the $Cu^{\delta+}$-Cu^0 synergy at the grain boundaries[20]. Nilsson *et al.* further revealed the presence of residual oxygen under the eCO_2RR conditions by combined spectroscopic and microscopic findings[21]. However, the detailed correlation between the dynamic structural change and catalytic reactivities has not been extensively investigated in these studies. Deciphering these pivotal structure-reactivity correlations in ODC materials should facilitate the rational design of electrocatalysts with improved C_{2+} product selectivity.

Vastly improved modern instrumentation has given us more reliable and convenient access to revealing the reaction mechanism and hence allows more rational approaches for catalyst optimization. Conventional *operando* characterization has often benefitted using synchrotron X-ray with ultra-high beam brilliance, which can overcome the intrinsic limitations in reactor cell design. For instance, our team have recently designed an *operando* reactor cell that allows the powder X-ray diffraction (PXRD) investigation of an electrode fully immersed in KOH electrolyte[22]. The access to synchrotron facilities is, however, generally limited, which hampers such important catalyst characterization under *operando* conditions. It would therefore be highly beneficial to fully utilize standard in-house laboratory capabilities for analogous *operando*

investigation. Very recently, Yang *et al*. reported that highly polycrystalline Cu nanograins can offer uncoordinated active sites to promote C_{2+} formation by *operando* electrochemical scanning transmission electron microscopy[23]. Here we further investigate the Cu^{+}/Cu^{0} synergy by studying the correlations between the structure of the electrocatalysts and the eCO_2RR activity during eCO_2RR. This study employs a series of model Cu_2O nanocrystals with octahedral, cubic, and nanowire morphologies (denoted as 'O-Cu_2O', 'C-Cu_2O', and 'N-Cu_2O'). KCl electrolyte (instead of the more commonly used $KHCO_3$) is used as the presence of surface Cl^- has been shown effective in deterring the rate of electrochemical reduction of ODC catalysts[24]. By conducting a series of multi-modal *operando* studies (**Scheme 1**), the dynamic changes in the bulk (by *operando* PXRD), surface/sub-surface (by *operando* Raman spectroscopy), and interface properties (by *operando* Fourier-transform infrared (FTIR) spectroscopy) with respect to the eCO_2RR performance have been revealed. In brief, O-Cu_2O generates the most intricate and long-lasting Cu_2O/Cu grain network under operating conditions. The intricate network of Cu_2O/Cu grain boundaries shows a positive correlation with the product selectivity toward ethylene.

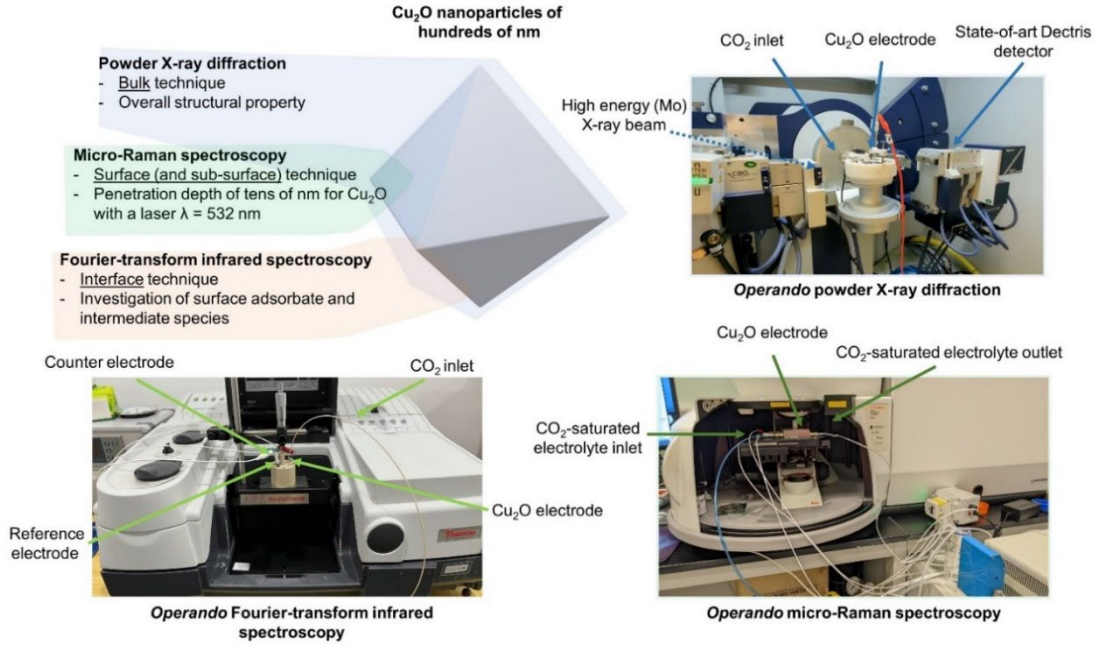

Scheme 1. Core *operando* characterization techniques used in this work, where the bulk and interface properties of the Cu_2O nanoparticles can be simultaneously studied. The designs of the reactor cells are illustrated in **Figures S1–S3**.

2. Results and Discussion

O-Cu_2O and C-Cu_2O were synthesized by a modified water bath method at pH 8.5 and 13, respectively. N-Cu_2O was prepared by applying *o*-anisidine to suppress the transverse growth of the crystals. The detailed synthesis procedures are summarized in Methods in Supplementary Information (SI). High-resolution scanning electron microscopy (SEM) images of the Cu_2O nanocrystals are shown in **Figure 1**, where clear octahedra, cubes, and nanowires can be seen. The O- and C-Cu_2O nanoparticles are of comparable apparent particle sizes of around 400 nm. The width of N-Cu_2O is around 50 nm.

PXRD measurements reveal the high sample crystallinity of all three Cu_2O nanocrystals. All the Cu_2O nanocrystals are cubic with the space group of *Pn-3m*. By applying the Pawley refinement, the unit cell parameters (*a*) for O-, C-, and N-Cu_2O were determined as 4.26832(1) Å, 4.26712(1) Å, and 4.27140(10) Å, respectively (see **Table S1** in the SI). N-Cu_2O possesses a larger unit cell, which could be attributed to the high surface-to-volume ratio and its unique nanowire structure that has a more exposed surface along one direction. From the quantitative analysis of the Bragg peaks for O- and C-Cu_2O, the size distributions are highly homogeneous with estimated crystallite domains of 70(2) and 72(2) nm, respectively. Similarly, the size of the crystallite domains of N-Cu_2O has been estimated at 50(2) nm. The graphical interpretation between apparent particle size (from SEM) and crystallite domain (from PXRD) is accordingly presented in **Figure 1**, where each 'apparent' nanoparticle is comprised of multiple nanocrystalline domains. The oxidation states of +1 in all three nanocrystals were confirmed by X-ray absorption near edge spectroscopy (**Figure S4**). The quantitative analyses of the extended X-ray absorption fine structure (EXAFS) spectra are shown in **Figures S5–S7**, with the backscattering of Cu–O and Cu–Cu at around 1.84 Å and 3.01 Å, respectively (detailed information is summarized in **Table S2**). These bond lengths agree with the typical literature values of Cu_2O[25]. Highly

comparable local structures are also evident from the corresponding wavelet spectra as shown in **Figure S8**.

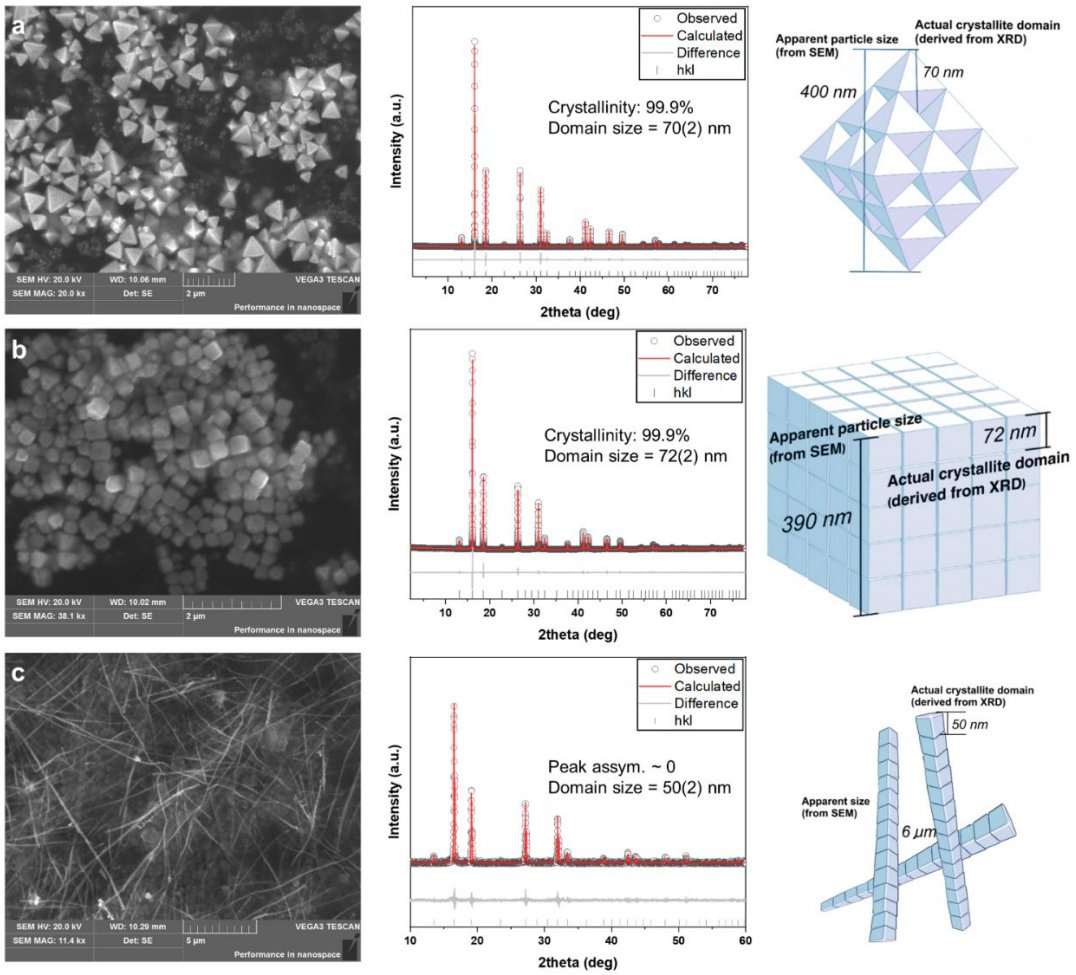

Figure 1. High-resolution SEM images of as-synthesized (**a**) O-Cu_2O, (**b**) C-Cu_2O, and (**c**) N-Cu_2O, and the corresponding synchrotron PXRD (**a–b**, Energy = 18 keV and wavelength = 0.688606 Å; collected in BL02B2 at SPring-8) and PXRD (**c**, Mo-$K_{\alpha1}$ = 0.70930 Å) patterns. The crystallographic parameters are summarized in **Table S1.**

The eCO_2RR catalytic measurements were conducted over these Cu_2O nanocrystals. All the electrochemical measurements were performed at the applied potential of −1.1 V vs RHE in a standard H-cell arrangement (see Methods/SI for the experimental details). The Cu_2O nanocrystals were first dispersed in Nafion-isopropanol solution (0.5‰), which were subsequently deposited on a carbon fiber paper at 1.00 mg cm^{-2}. Similarly, the electrolyte was maintained at the cathodic side of the H-cell at the CO_2 purging rate of 20 sccm.

The basic electrochemical properties of the Cu_2O nanocrystals were studied by conventional electrochemical measurements. As shown in the linear sweep

voltammetry curves (**Figure S9a–c**), the current densities in all three nanocrystals increased noticeably in the CO_2-saturated KCl electrolyte, which indicates their electrochemical activity with CO_2. The equivalent resistance (in terms of Rct and RΩ) of the nanocrystals has been studied by electrical impedance spectroscopy (**Figure S9d**), with O-Cu_2O having the lowest resistance among the three Cu_2O nanocrystals[26,27]. The double-layer capacitance and the corresponding electrochemically active surface areas were obtained from cyclic voltammetry measurements at different scan rates (**Figure S10a–c**). The charging currents Δj at 0.545 V vs RHE were plotted against the scan rates (**Figure S10d**). The electrochemically active surface areas were accordingly derived at 0.026 mF cm^{-2} for O-Cu_2O, 0.089 mF cm^{-2} for C-Cu_2O, and 0.006 mF cm^{-2} for N-Cu_2O.

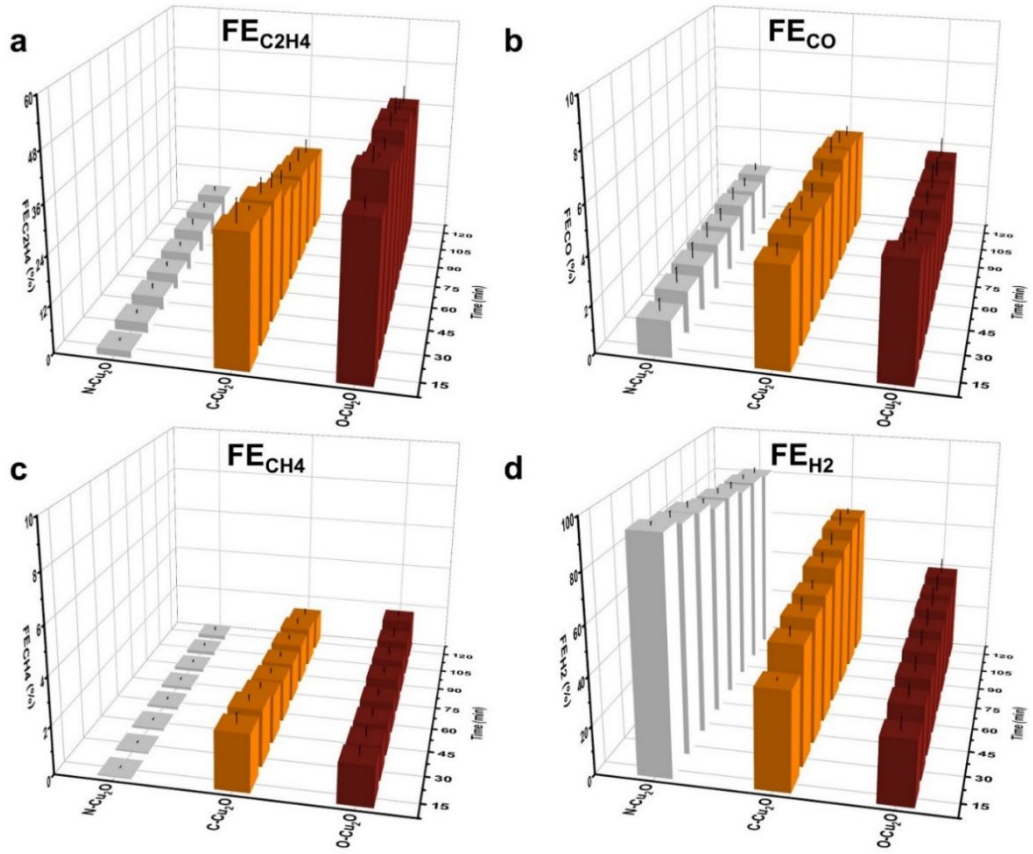

Figure 2. Calculated FEs of the major gaseous eCO_2RR products (**a**) C_2H_4, (**b**) CO, (**c**) CH_4, and (**d**) H_2 from the catalytic measurement over 2 hours of time-on-stream. The eCO_2RR measurements were conducted at –1.1 V vs RHE. 1.0 M KCl was used as the electrolyte. The corresponding chronoamperometric curves are shown in **Figure S11d**.

Figure 2a–c shows the time-resolved evolution of the Faradaic efficiencies (FEs) of the major gaseous products at –1.1 V vs RHE over O-, C-, and N-Cu_2O measured at every 15-minute interval by gas chromatography. We observed three major gaseous

products from eCO_2RR, namely, CO, CH_4, and C_2H_4. The FE values are in high agreement with a recent study by Luo *et al*, which also studied Cu_2O with related morphologies[28]. O-Cu_2O showed the highest production of C_2H_4 at around 40%, where the FE_{C2H4} remained stable for 2 hours of time-on-stream. In contrast, the FE_{C2H4} decreased from 33% to 20% over C-Cu_2O in two hours, whereas that of N-Cu_2O remained low at *ca*. 5%. The corresponding plots of FE_{H2} from the hydrogen evolution reaction are summarized in **Figure 2d**. Interestingly, coherent with the time-resolved eCO_2RR findings, the decreased production of C_2H_4 over C-Cu_2O was approximately offset by a similar increase in the production of H_2 (from FE_{H2} of 41% to 66%). We did not include the liquid products in the main text for discussion, as they only constitute a much smaller part of the product distribution (see the characterization of liquid products by NMR summarized in **Figure S12 and Table S3**). The low values of FE_{C2H4} and high value of FE_{H2} over N-Cu_2O obtained in our catalytic system were verified by multiple experiment attempts, which could be due to various intrinsic reasons, *e.g.*, the lower ability to form surface oxygen species and keep high *CO intermediate concentration on the catalyst surface[29,30]. Indeed, extremely low production of C_2H_4 has also been observed over 'perfect' polycrystalline Cu surfaces in the absence of native oxygen species[31]. Briefly, O-Cu_2O is the best-performing eCO_2RR catalyst in terms of FE_{C2H4} among the three Cu_2O nanocrystals. It is, therefore, worth investigating the origins of the difference in reactivity over these structurally related Cu_2O nanocrystals. The morphologies of all the catalysts were maintained to a large extent, as seen in the post-mortem microscopic images in **Figures S13–S14**. However, it is difficult to decipher the correlations between the structural and catalytic properties based on conventional *ex-situ* or even *pseudo-in-situ* approaches due to the oxygen sensitivity of the as-reduced metallic Cu species and other meta-stable species when the reducing potential is lifted. We have also conducted a series of *pseudo-in-situ* PXRD measurements (protected once reducing potential is lifted at different points in time), as shown in **Figure S15,** which show different profiles when compared with our *operando* PXRD measurements (as later discussed). Hence, complex-but-operando measurements are needed for truly dynamic investigations on the structural evolution of the catalysts.

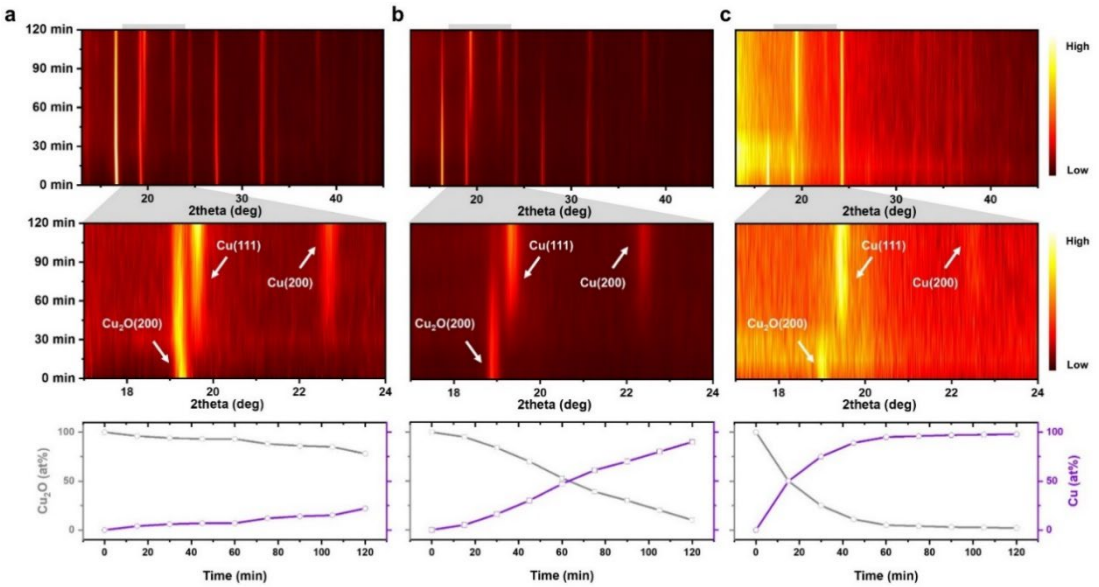

Figure 3. (**Top**) Two-dimensional contour profiles of operando PXRD measurements of (**a**) O-Cu_2O, (**b**) C-Cu_2O, (**c**) N-Cu_2O, and their zoom-in profiles showing the 2θ range between 17° and 24°, covering the Cu_2O(220), Cu_2O(111) and Cu(200) reflections. (**Bottom**) Quantitative analysis of the crystalline phases Cu and Cu_2O calculated from the whole-pattern refinement using the Rietveld method.

We, here, adopted a multi-modal *operando* characterization approach as illustrated in **Scheme 1**. It allows us to simultaneously investigate the bulk, surface (and sub-surface), and interface properties of the Cu_2O nanocrystals under comparable reaction conditions, which offers a much more comprehensive analysis than using *operando* characterization techniques independently. Lei *et al*. have also adopted an analogous philosophy to study the lattice strain effect of various Cu catalysts under electrochemical conditions[32]. In this regard, we have specifically designed a series of reactor cells where the design drawings are presented in **Figures S1–S3**. In particular, an *operando* electrochemical reactor cell was developed with the technical team of Beamline I11 at Diamond Light Source (UK) to allow PXRD measurements under applied potential with flowing CO_2. A high signal-to-noise ratio has been ensured by minimizing direct contact between the X-ray beam and electrolyte.

The time-resolved PXRD two-dimensional contour plots of the three Cu_2O under *operando* conditions are presented in **Figure 3**, with the individual PXRD patterns shown in **Figures S16─S18**. Note that the peak at 2θ = 24.2° is characteristic of the carbon fiber paper, which was also used as an internal standard to ensure the precision of the *operando* measurements. We observed noticeably different time-resolved PXRD profiles over the three Cu_2O electrocatalysts (the Rietveld refinement profiles are

plotted in **Figures S19─S21**). The dynamic change in the PXRD profiles over time is associated with the electrochemical reduction of Cu_2O to the metallic Cu phase, as seen in the fingerprint labeling. Clearly, the kinetic profiles of the electrochemical reduction of Cu_2O to Cu are different. As seen in our zoom-in displays, the most notable changing features from the diffraction profiles can be observed at 2θ of 19.1°, 19.6°, and 22.6°, which correspond to $Cu_2O(200)$, Cu(111), and Cu(200), respectively. Clearly, N-Cu_2O showed the most rapid electrochemical reduction, which can be attributed to the notably higher surface-to-volume ratio of the nanowire morphology. In contrast, the rates of electrochemical reduction of O-Cu_2O and C-Cu_2O were much lower. A dominant Cu_2O phase was still present after 120 minutes of time-on-stream. No Bragg peak characteristic of $Cu(OH)_x$ was detected during the eCO_2RR, indicating that these species, if present, were in the ultra-fine or amorphous phases.

Upon electrochemical reduction, the unit cell parameters of the newly formed metallic Cu are 3.621(1) Å, 3.619(10) Å, and 3.627(9) Å, respectively. Using the broadening model for peak profiles by the Rietveld method, the size of the extrapolated crystallite domains of Cu decreases substantially from *ca.* 70 nm to 18 nm for the O- and C-Cu_2O nanocrystals (consistent with our post-mortem TEM results as shown in **Figure S14**), but the size of the N-Cu_2O domains remained relatively unchanged. It suggests that the O- and N-Cu_2O crystallite domains (constituents of a larger nanoparticle) were converted to smaller metallic Cu domains because of potential nanocrystallite fragmentation and lattice shrinkage[32]. It should be noted that the instrumental effect on the extrapolation of the domain sizes has been carefully corrected by using Si standard (NIST SRM640e) as done before[33]. A graphical representation of this structural transformation is presented in **Scheme 2**, which will be discussed later.

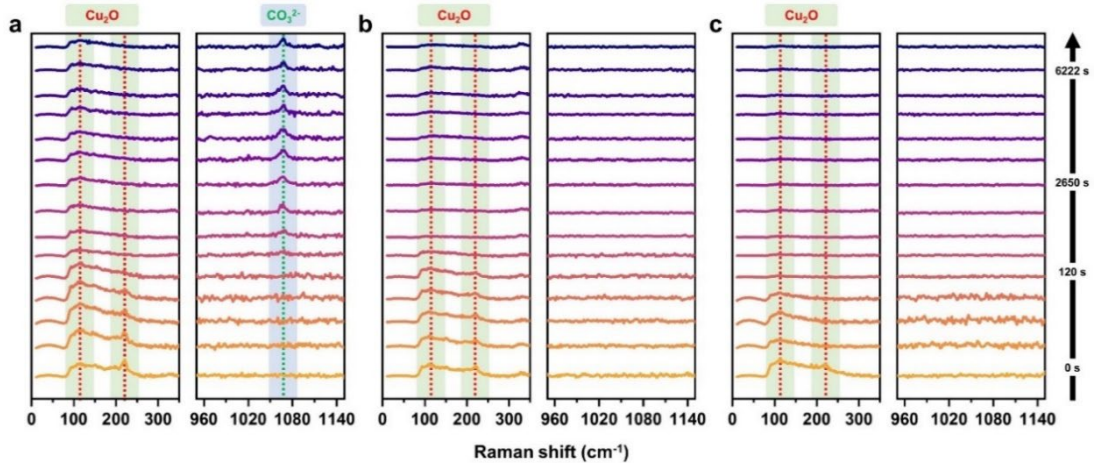

Figure 4. *Operando* micro-Raman spectroscopic measurements collected at –1.1 V vs RHE in CO_2-saturated 1.0 M KCl electrolyte for (**a**) O-Cu_2O, (**b**) C-Cu_2O, and (**c**) N-Cu_2O.

A quantitative analysis of the concentrations of the crystalline phases of Cu and Cu_2O from the *operando* PXRD measurements using the Rietveld method has been subsequently conducted, as shown in **Figure 3 (bottom)**. First, it can be noted that the electrochemical reduction of O-Cu_2O to metallic Cu was the slowest, with only around 10% Cu_2O crystallite domains reduced to form metallic Cu domains after one hour of time-on-stream and 22% Cu_2O reduced after two hours (*cf*. Cu: Cu_2O = 0.28). The rate of electrochemical reduction of C-Cu_2O was faster, with about 50% Cu_2O converted after one hour and around 90% converted after two hours (*cf*. Cu: Cu_2O = 8.9). In stark contrast, almost half of N-Cu_2O was converted after 15 minutes, and almost complete conversion (>98%) of N-Cu_2O is noted after one hour of time-on-stream. The rapid electrochemical reduction of N-Cu_2O falls within our expectations as N-Cu_2O has a much higher surface-to-volume ratio compared with O- and C-Cu_2O. The relative resistance of O- and C-Cu_2O upon applied potential could also be related to their larger unit cells (*cf*. ~ 4.34 Å for O- and C-Cu_2O; ~ 4.28 Å for N-Cu_2O and common literature values[5,34]). It should be noted that the current quantitative phase analysis has only considered crystalline Cu and Cu_2O phases. Although we only detected minimal change in the background scattering and did not detect any Bragg peaks characteristic of $Cu(OH)_x$, the possible presence of metastable, short-lived, amorphous oxidized species in the sample under such dynamic measurement still cannot be excluded.

As discussed above, Cu_2O nanocrystals with different morphologies underwent electrochemical reduction at different rates from the bulk material point of view. We have further employed *operando* micro-Raman spectroscopy to elucidate the surface and sub-surface properties during eCO_2RR. We have particularly chosen a green laser (λ = 532 nm) as its penetration depth into Cu/Cu_2O is around tens of nm[35]. The Raman spectra were measured at an interval of at least ten seconds to reduce inelastic light scattering, which would influence the peak intensity[18]. The laser can penetrate through a thin layer of typical electrolytes with low Raman scattering cross-sections[36]. Low Raman scattering cross sections would allow reliable characterization of the electrode/electrolytes interface, where electrolysis takes place.

The *operando* micro-Raman spectra are displayed in **Figure 4**. At the start of the experiment (t = 0 s), we noted a series of fingerprint vibrational peaks corresponding to Cu_2O. The peaks at 144 cm^{-1} and 215 cm^{-1} correspond to the Raman scattering from phenon symmetry Γ^{-}_{15} and second-order Raman mode, respectively[37]. These Cu_2O-related Raman peaks became noticeably weaker upon applied potentials, which can be

attributed to the rapid electrochemical reduction of the surface and sub-surface layers of Cu_2O. The contribution of O-Cu_2O at 144 cm^{-1} only decreased marginally, with the peak intensity maintaining at about half the initial value after two hours of time-on-stream. In particular, it contrasts with that of N-Cu_2O, where the Cu_2O Raman contribution disappeared simply after a few minutes, and that of C-Cu_2O with about 10% intensity remains after two hours. In brief, the Cu_2O-related Raman intensity decreased in the following order: N-Cu_2O > C-Cu_2O > O-Cu_2O. This hence indicates that not only the bulk but also the surface and sub-surface of O-Cu_2O are more sluggish upon electrochemical reduction. We did not detect any noticeable Raman peaks at around 535 and 602 cm^{-1}, which infers the absence of CuO_x species[38]. The findings based on this *operando* Raman spectroscopic study exhibit a high resemblance with those obtained above from *operando* PXRD.

Meanwhile, we also noted the appearance of a new Raman peak at 1074 cm^{-1} over O-Cu_2O after one minute of time-on-stream, which can correspond to the stretching mode of adsorbed CO_3^{2-} on the catalyst surface[39]. Typically, this adsorbed CO_3^{2-} species can be related to the increased concentration of reducible CO_2 in the solution near the electrode surface through rapid equilibrium exchange between aqueous CO_2 and CO_3^{2-}. Interestingly, this CO_3^{2-} peak is only observed over O-Cu_2O but not over N- or C-Cu_2O, which could infer that the concentration of adsorbed CO_2 is much higher on the surface of O-Cu_2O.

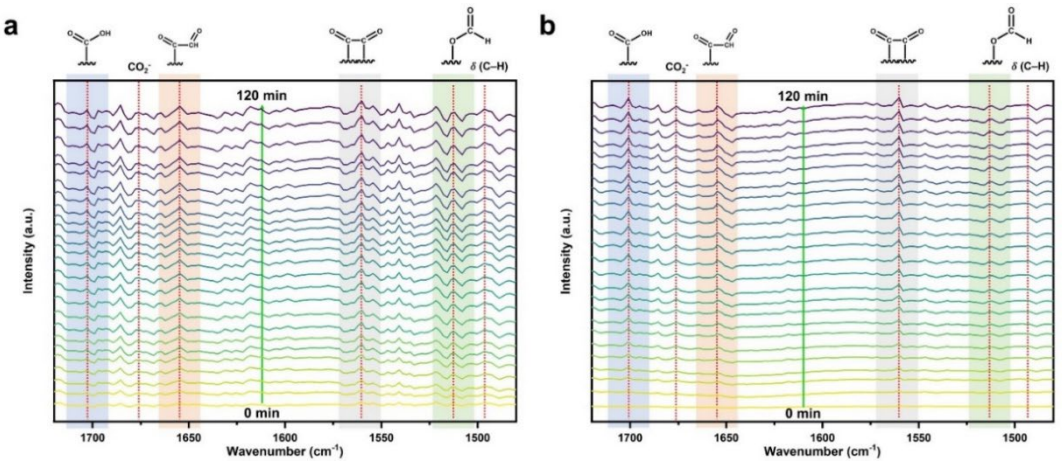

Figure 5. *Operando* FTIR spectra of (**a**) O-Cu_2O and (**b**) C-Cu_2O measured at –1.1 V vs RHE in CO_2-saturated 1.0 M KCl aqueous solution. The presence and formation of various intermediate species are highlighted.

We then employed *operando* FTIR spectroscopy to study the surface adsorbates and reaction mechanism over O-Cu_2O and C-Cu_2O as they are the more presentative samples. As shown in **Figure 5**, the *operando* FTIR spectra were collected at every 5 minutes interval at –1.1 V vs RHE, with the full range data and further zoom-in illustration plotted in **Figures S22–S23**. A series of adsorbed CO_2 and activated CO_2 species can be observed, such as the band at 1518 cm^{-1} attributed to adsorbed *OCOH species, 1676 cm^{-1} attributed to CO_2^-, and 1705 cm^{-1} attributed to *COOH[40]. It is understood that CO_2 will first be reduced to form activated *CO on the surface that can subsequently dimerize to form *OCCO and reduce to form *OCCHO to produce C_{2+} products electrochemically, often called the CO dimerization pathway[41]. The IR peaks at 1560 cm^{-1} and 1651 cm^{-1} can be attributed to asymmetric ν_{co} stretching of *OCCO and asymmetric ν_{co} stretching of *OCCHO, offering evidence for the CO dimerization pathway, which agrees with previous findings[42]. Similar observations about the detection of the intermediate species (towards C_2H_4) from the measurements over O- and C-Cu_2O were obtained. This falls within our expectations as C_2H_4 is a major product over the time-on-stream over both catalysts. However, as the quantification of these species using FTIR is challenging, it is intrinsically difficult to yield comparable analyses between these catalysts as the difference in product formation is relatively minor.

Based on the above results, we can accordingly establish the correlations between the dynamic structural change and the corresponding catalytic properties, as shown in **Scheme 2**. In brief, O-Cu_2O was the best-performing eCO_2RR catalyst among the three

Cu_2O nanocrystals studied with different morphologies in terms of relatively higher FE_{C2H4} and higher stability in production. Meanwhile, for C-Cu_2O, the FE_{C2H4} at the early stage was comparable to those of O-Cu_2O, but it decreases notably over time, rendering a much less stable production of C_2H_4. In N-Cu_2O, the electrochemical reduction process under applied potential was rapid, which suggests that the catalytic reaction could be primarily nanowire Cu-metal driven. Different reduction profiles of these Cu_2O nanocrystals were noticed, which can be attributed to the difference in surface energies that is dependent on the local atomic arrangement[43].

The observed reduction behaviors do not fully reflect typical thermodynamical interpretations, where rapid and complete Cu_2O reduction would be expected. In general, the reduced metallic Cu species should be conductive, which could further facilitate the reduction process. In our study, the use of KCl as the electrolyte may have lowered the rate of reduction due to the presence of Cl^-[24]. Based on our *operando* PXRD studies on the crystallite domains, the crystallite Cu_2O domains generally remains at around 60–70 nm even though their concentrations decrease at different extent upon electrolysis. Smaller Cu domains (at < 20 nm) are formed from *in-situ* reduction, reconstruction, and fragmentation of Cu_2O during electrolysis. This agrees with the conventional understanding that the standard electrode potential would change significantly when the size of the nanocrystals decreases from the bulk to the atomic regime. It suggests that the thermodynamics for the formation of crystallite Cu domains is greatly related to the size of the domains. The electrochemical reduction of Cu_2O to Cu is known to create lattice strain[32] and local defective structures[43], which decreases the stability and affects the energy of surface Cu atoms of the as-formed metallic Cu domains. Our findings are consistent with that reported by Huang *et al.*, where the formation of small Cu domains is preferable with a surface Cu site with low coordination under the eCO_2RR conditions[44].

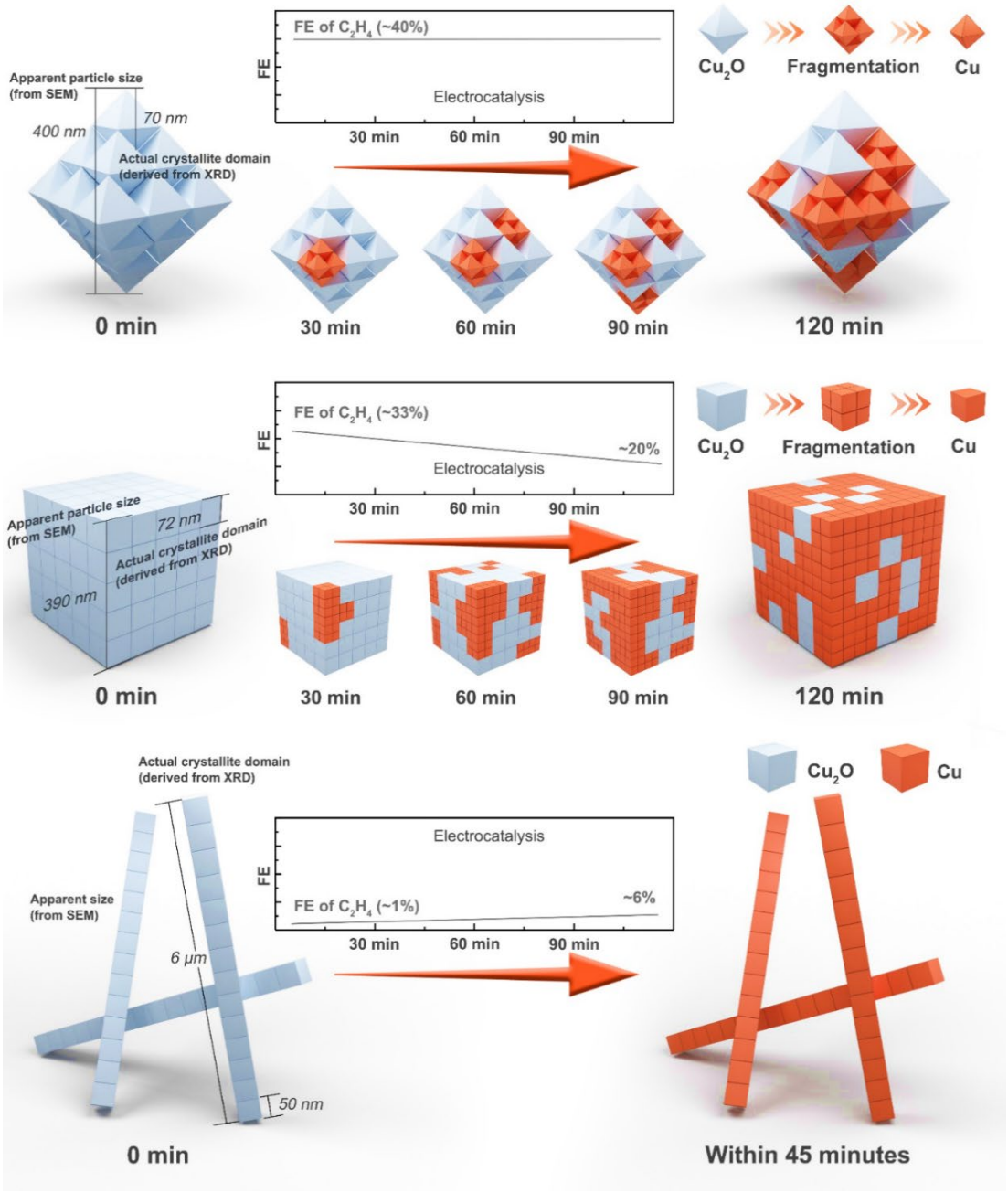

Scheme 2. Schematic illustration of the structure-reactivity correlations established based on the multi-modal *operando* characterization and catalytic results over the O-, C-, and N-Cu_2O nanocrystals.

Based on the theoretical study by Goddard III *et al.*, the synergy between surface Cu^+ (in Cu_2O) and Cu^0 (in metallic Cu) can greatly favor activated $*CO_2$ species for C─C coupling, affording multi-carbon products[45]. As proposed by Verdaguer-Casadevall *et al.*, interconnected newly generated Cu domains can stabilize the Cu_2O/Cu^0 grain boundary and defect terminations, which could increase the population of $Cu^{\delta+}$–Cu^0 junctions[46]. As illustrated in **Scheme 2**, O-Cu_2O delivers a more intricate network of Cu_2O/Cu (and hence Cu^+-Cu^0 junctions) upon electrochemical reduction compared

with C-Cu_2O. We have accordingly employed density functional theory (DFT) calculations to investigate how these structural changes affect the *d*-band centers and their corresponding effects on the product selectivities. We employed O- and C-Cu_2O as the model compounds for a fair comparison due to their similar structural characteristics. The projected density of states (PDOS) of the *d*-band centers of Cu and Cu_2O, with exposed (111) and (100) facets, are presented in **Figure 6a–d**. The *d*-band centers of Cu, derived from O- and C-Cu_2O, are highly comparable at –2.33 eV, but those of Cu_2O are notably different at –2.09 eV for O-Cu_2O and –1.91 eV for C-Cu_2O. As shown in **Figure 6e–h**, the *d*-band centers of combined Cu_2O and Cu phases ('Cu_2O/Cu') are subsequently different at –2.01 eV for Cu_2O(111)/Cu(111) and –2.06 eV for Cu_2O(100)/Cu(100). The side views of the crystal slabs are presented in **Figure S24**. This suggests that the *d*-band center can be relatively maintained at the same level in O-Cu_2O, but notably downshifted in C-Cu_2O. The downshifted *d*-band center (further away from the Fermi level) weakens the binding of CO* intermediate[47,48]. It suggested that the combination of Cu_2O/Cu in C-Cu_2O would impede the eCO_2RR performance. Indeed, it is verified in our catalytic results where the FE_{C2H4} over C-Cu_2O kept falling during the eCO_2RR (from 33% to 20%), whereas the FE_{C2H4} over C-Cu_2O remains relatively constant over time (~40%).

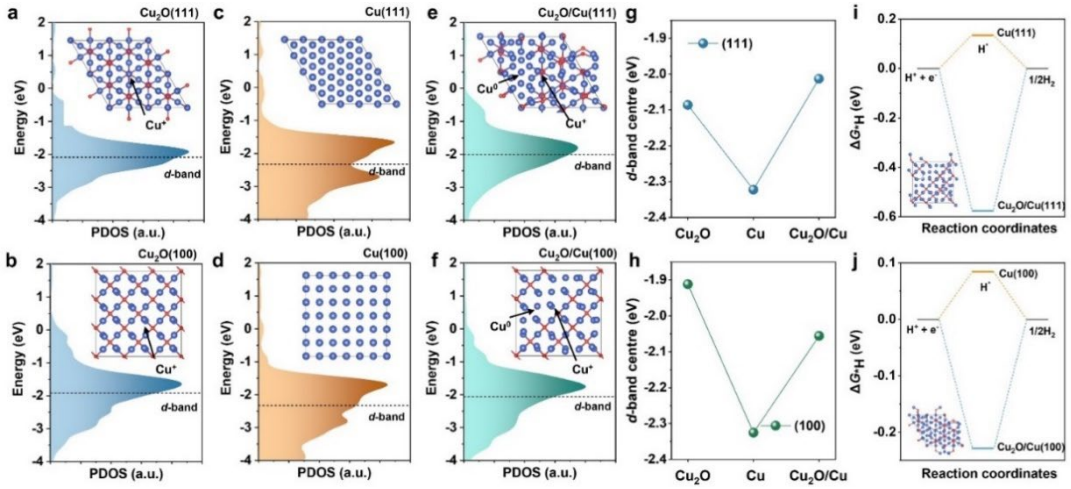

Figure 6. Projected density of states (PDOS) of the *d*-band for (**a, b**) O- and C-Cu_2O and (**c, d**) Cu and (**e, f**) Cu_2O/Cu with the surface orientation of (111) and (100), respectively. The horizontal black dashed lines indicate the positions of the *d*-band center (referenced to the Fermi level at zero). Insets are top views of the corresponding crystal slab structures. (**g, h**) Calculated *d*-band centers for **a–f**. All the calculations were performed at GGA/PBE level. Calculated adsorption free energy of *H (ΔG_{*H}) on

(**i**) Cu(111) and Cu_2O(111)/Cu(111) and (**j**) Cu(100) and Cu_2O(100)/Cu(100). Insets are top views of the crystal slab structures with an *H adsorption.

Another interesting observation from our catalytic results is that the FE_{H2} over C-Cu_2O increases noticeably over time (from 41% to 66%). We have further employed DFT calculations to study the tendency of hydrogen evolution reaction (HER) over O- and C-Cu_2O as the catalysts evolve. As shown in **Figure 6i**–**j**, the plot of reaction coordinates shows the difference in the respective adsorption free energy of *H (ΔG_{*H}) on Cu_2O/Cu and Cu. The adsorption of H* in Cu_2O(111)/Cu(111) is –0.58 eV, which is much more thermodynamically stable compared to that of Cu_2O(100)/Cu(100) at –0.29 eV. This suggests that the barrier for HER over Cu_2O(111)/Cu(111) is much larger than that of Cu_2O(100)/Cu(100). HER over the mixed Cu_2O(100)/Cu(100) phase is, thus, relatively favored. It is in great agreement with our catalytic findings where the FE_{H2} increases notably from 41% to 66% over C-Cu_2O but that over O-Cu_2O remains relatively stable at 30%.

Briefly, the upshifted *d*-band center of Cu_2O/Cu with an exposed facet of (111) in O-Cu_2O is the most conducive toward the production of ethylene, whereas the downshifted *d*-band center of Cu_2O/Cu in C-Cu_2O leads to a decreased production of C_2H_4 in the expense of increased H_2. The modeling study is highly supportive of what has been proposed in the literature (about the synergy of Cu^+-Cu^0 junctions primarily based on computational understanding)[49,50], and our derived structure-activity correlations (that O-Cu_2O can offer a more stable and efficient production of C_2H_4).

3. Conclusion

In summary, we have revealed the structure-reactivity correlations by investigating the dynamic change of the bulk, surface (and sub-surface), and interface characteristics of the crystallite domains of various Cu_2O nanocrystals with regard to the catalytic properties. The rate and extent of electrochemical reduction of O-, C-, and N-Cu_2O under eCO_2RR conditions were notably different, with O-Cu_2O reduced at the slowest rate among Cu_2O with three different morphologies studied. By adopting a multi-modal *operando* characterization philosophy, we discovered the formation of an intricate network of Cu_2O/Cu grain boundaries (and hence Cu^+-Cu^0 junctions) from *in-situ* electrochemical reduction. Although at this current stage, we still cannot accurately predict or estimate the optimal Cu: Cu_2O ratio. The synergy along the Cu_2O/Cu grain boundaries in O-Cu_2O was found the most favorable for ethylene production from the eCO_2RR. The *in-situ* electrochemical reduction can indeed be regarded as an activation for Cu-based catalysts *via* surface and bulk reconstruction instead of deactivation.

The capacity of two highly complementary *operando* techniques has been clearly illustrated in this work, with the bulk, surface (and sub-surface), and interface properties studied. The development of laboratory-scale (non-synchrotron) reactor cells, more importantly, under comparable reaction conditions, can make the real-time characterization of electrocatalysts more facile and reliable. However, we should still carefully consider the intrinsic limitations of these techniques, for instance, the quantitative analysis of crystalline phases with the potential presence of amorphous Cu phase, during experiment design and data interpretation.

4. Materials and method

4.1 Experimental Procedures

4.1.1 Materials

Copper(II) sulfate pentahydrate (98%), copper(II) acetate (99%), sodium hydroxide (97%), sodium ascorbate (99%), potassium chloride (99.8%), and Nafion 115 dispersion (5% in water and 1-propanol) were obtained from Sigma-Aldrich. Ethanol (AR), isopropanol (AR), and hexane (AR) were purchased from Sinopharm Chemical Reagent Corporation. Oleic acid (AR) was purchased from Aladdin. Hydrophobic carbon paper (TGP-H-60) was purchased from Toray Corporation. O-anisidine was purchased from Alfa Aesar. All chemicals were directly put into use without further purification.

4.1.2 Synthesis of cuprous oxide nanocrystals

The cubic (C-Cu_2O) and octahedral (O-Cu_2O) Cu_2O nanocrystals were synthesized by a modified method[51,52]. Firstly, 0.1 M of the aqueous solution of Cu_2SO_4 (10 mL), distilled water (67 mL), and oleic acid (5 mL) were added to a flask. The solution was then separated into two phases, with the water phase on the bottom and the oil phase on the top. The solution was stirred in a water bath at 50 °C. When the oil phase turned blue, the aqueous solution of 1.0 M NaOH (14 mL) was added to the mixed solution in a flask quickly. After stirring for 15 min, while the solution turned into an emulsion with blue color, 0.1 M sodium ascorbate was added to adjust the pH value to 8.5. The flask was kept in the water bath for another 60 min with constant stirring. The O-Cu_2O was collected by centrifugation at 6000 rpm and washed six times with ethanol and hexane. Finally, the product was vacuum dried at room temperature for further use. The synthesis of C-Cu_2O was similar to that of O-Cu_2O. By adjusting the added amounts of 1.0 M NaOH solution to turn the pH value of the mixture solution to 13, C-Cu_2O could be obtained. The nanowire Cu_2O (N-Cu_2O) nanocrystal was prepared according to another previously reported method[53]. In a typical synthesis, 0.2 g of copper(II) acetate was dissolved in 40 mL of deionized water, followed by the addition of 80 μL of *o*-anisidine. The mixture was stirred for 5 min to form an olive-green solution. The solution was transferred into a 50 mL Teflon-lined stainless autoclave. After maintaining at 200 °C for 10 h, N-Cu_2O was obtained by centrifugation at 3000 rpm and washed with ethanol and DI water several times.

4.1.3 eCO_2RR Cathode Preparation

A homogeneous ink for the electrochemical measurement was prepared by mixing 10 mg of the catalyst into 1.0 mL of a Nafion-isopropanol solution (0.5‰), followed by sonication for 30 min. The electrode was prepared by loading the ink onto a carbon paper electrode (1 cm × 2 cm, the practically immersing area in the electrolyte was 1 cm × 1 cm) and drying under ambient conditions at 60 °C for 6 h with a loading of 1 mg/cm^2.

4.2 Method

4.2.1 Extended X-ray absorption fine structure spectroscopy

We obtained the X-ray absorption near edge structure (XANES) and extended X-ray absorption fine structure (EXAFS) spectroscopy data at BL07A at Taiwan Light Source using fluorescence mode, with an average scanning time of 20 minutes. Data fitting and analysis results were obtained by using Artemis and Athena software. The detailed fitting results are summarized in Table S2[54]. The Hamma software was used for wavelet transformation[55].

4.2.2 Electrochemical CO_2RR Measurements

eCO_2RR experiments were performed in a typical H-cell arrangement separated by a Nafion 115 membrane. The electrochemical measurements were conducted by a CHI 760E electrochemical analyser (Shanghai, Chenhua Co., China) in a three-electrode cell containing 1 M KCl electrolyte. Typically, an Ag/AgCl (in saturated KCl electrolyte) electrode was used as the reference electrode and a carbon electrode as the counter electrode. Before CO_2RR measurement, the electrolyte was pre-saturated with high-purity CO_2 for 30 min with a flow rate of 60 standard cubic centimetres per minute (sccm) controlled by a mass flow controller (model FMA-A2305) purchased from OMEGA Co, Ltd. All potentials were calibrated to an RHE by calculation. For the eCO_2RR experiment, a potentiostat test was conducted for 2 h in a CO_2-saturated 1 M KCl solution (35 mL) under atmospheric pressure and constant temperature. High-pure CO_2 was continuously purged in the cathode compartment under a constant flow rate of 20 sccm using a mass flow controller during the entire experimental process at the ambient conditions of 298 K and 1 bar. For gas chromatography, we employed a flame ionization detector (FID) and thermal conductivity detector (TCD) to measure the gas products using high-purity nitrogen gas (99.99%, Linde) as the carrier gas FID uses a TDX-01 column for CO, CH_4 and C_2H_4 measurement and TCD uses 6 feet MolSieve 5A mesh columns to detect the concentration of H_2. Furthermore, the column oven temperature is 70 °C.

The Faradaic efficiency (FE) of gas products was calculated using the following formula:

$$FE_{gas}(\%)=(zFG\rho)/(V_m \times i_{total})\times 100$$

where Z is the number of electrons transferred, F is Faraday's constant (96485 C/mol^{-1}), G is the flow rate of gas (20 sccm). ρ is the molar fraction of the product, V_m is the standard gas molar volume (24 L/mol), and i_{total} is the total current.

The liquid products were quantified using a Bruker Advance-III NMR spectrometer. 540 μL electrolyte collected from the cathode part of the H-cell was mixed with 60 μL D_2O containing 50 ppm dimethyl sulfoxide was used as the measurement sample. The ^1H spectrum was obtained via a water suppression method.

Since the concentration of DMSO, which is regarded as the internal standard, is known, the concentration of products also could be obtained by comparing their relative peak area to that of DMSO. The FE of liquid products was calculated using the following formula.

$$FE_{liquid}(\%)=(zFn_{DMSO}av)/Q$$

where z is the number of electrons transferred, F is Faraday's constant, n_{DMSO} is the amount of DMSO used, a is the molar ratio of the products and DMSO, v is the ratio of total volume electrolyte in the cathode part of H-cell and the collected electrolyte, and Q is the total charge.

4.2.3 High-resolution synchrotron X-ray powder diffraction (SXRD) and Rietveld refinement

High-resolution SXRD data were collected at Beamline BL02B2, SPring-8, Japan. The energy of the incident X-ray flux was set at 18 keV. The tuned energy for each beamline emits the optimum X-ray flux to achieve high contrast (signal-to-noise ratio) and high angular resolution. The wavelength and the 2θ-zero point were calibrated using a diffraction pattern obtained from a high-quality standard CeO_2 powder. High-resolution SXRD data were obtained from the Cu_2O samples (loaded in 0.5-mm borosilicate capillaries) using the MYTHEN detector. Each diffraction pattern was collected for an hour for good statistics.

Using the TOPAS 6.0 software, the lattice parameters were obtained using Pawley and Rietveld refinement analyses of the diffraction patterns were performed. The background curve was fitted by a Chebyshev polynomial with an average of 16 coefficients. The Thompson-Cox-Hastings (pseudo-Voigt) function was applied to describe the diffraction peaks[56]. The scale factor and lattice parameters were allowed to vary for all the histograms.

The final refined structural parameters for each data histogram were carried out using the Rietveld method with the fractional coordinates (*x, y, z*) and isotropic displacement

factors (B_{eq}) for all atoms. In addition, the R_{wp} and *goodness-of-fit* values (*gof* = R_{wp}/R_{exp}) are helpful to indicate the quality of fit, where R_{exp} represents the quality of the data.

4.2.4 Operando PXRD measurement

Operando PXRD measurements were performed in a particular cell designed by our team. To obtain high signal-to-noise ratio, we used carbon fibre paper (low background) with a loading of 4 mg/cm^2 as the working electrode. A carbon and an Ag/AgCl (in saturated KCl) electrodes were used as the counter and reference electrodes respectively. And 1M KCl electrolyte was continuously purged with CO_2 throughout the experiment. High-energy X-ray (Mo anode) was used to optimize the spatial and angular resolution of Bragg's reflections. During the 2h-*operando* PXRD measurement, each PXRD pattern was required every 15 minutes for a suitable and reliable signal-to-noise ratio.

4.2.5 *Operando* Raman measurement

Operando Raman measurement is performed in a three-electrode follow cell purchased from GAOSHIRUILIAN, with being used carbon fibre paper as the working electrode. A carbon electrode and Ag/AgCl (in saturated KCl) were used as the counter electrode and reference electrode, respectively. We used the potentiostat method to perform the electrochemical measurement in CO_2-saturated 1M KCl electrolyte. And high purity CO_2 gas was continuously purged into the electrolyte with a flow rate of 20 sccm using a mass flow controller. The electrolyte was continuously circulated through the cell at a rate of 1 ml/min. Raman spectroscopy was carried out using an Avantes AvaRaman spectrometer equipped with an Intertec λ = 532 nm with 5% laser power as the excitation source. The Raman probe was focused on the electrode/electrolyte interface through a quartz window.

4.2.6 *Operando* FTIR measurement

A THERMO Nicolet 6700 spectrometer equipped with a liquid nitrogen-cooled MCT detector was used for *operando* FTIR measurement with the operating voltage at –1.1 V vs RHE Glass carbon electrode coated with catalyst (1 mg/cm^2) was used as the working electrode. An Ag/AgCl electrode and a carbon electrode were used as the reference and counter electrode, respectively. In addition, a silicon facet crystal with an incident angle of 60° was used as the reflective element (ATR mode). 1 M CO_2-saturated KCl solution was used as electrolyte.

4.2.7 DFT calculation method

We performed the density functional theory (DFT) calculations using the projector-augmented wave method as implemented in Vienna Ab initio Simulation Package (VASP)[57,58]. The generalized gradient approximation (GGA) with the Perdew-Burke-Ernzerhof (PBE) exchange-correlation functional was employed. A uniform 6×6×6 k-mesh grid in the Brillouin zone was used to optimize the crystal structure of bulk Cu and Cu_2O. The pristine Cu and Cu_2O slab models had a (2×2) lateral periodicity for (111) exposed surface and a (3×3) lateral periodicity for (100) exposed surface with a vacuum layer of ~20 Å. The Cu_2O/Cu(111) and Cu_2O/Cu(100) slabs containing Cu^0 and Cu^+ atoms on the top surface were constructed following the model for metal embedded in an oxidized matrix as proposed by Xiao *et al*.[45] A 2×2×1 k-mesh was used for all slab structures. The kinetic energy cutoff for the wave functions was set at 500 eV for the bulk and 450 eV for slab structures without and with $*H/H_2$ adsorption. The atomic positions of the top two layers in the slab structures were relaxed and other bottom layers were fixed (until the forces on each atom were less than 0.01 eV/Å). The optimized slab structures are shown in **Figure S24**.

The free energy for hydrogen adsorption (ΔG_{*H}) was calculated as

$$\Delta G_{*H} = E(\text{slab} + \text{H}) - E(\text{slab}) - E(\text{H}_2)/2 + \Delta E_{\text{ZPE}} - T\Delta S$$

where E(slab + H) and E(slab) are the total energies of the Cu_2O/Cu(111) or Cu_2O/Cu(100) slab with and without H adsorption; $E(H_2)$ is the total energy of an H_2 molecule; ΔE_{ZPE} is the difference in the zero-point energy (ZPE) between the gas phase of H_2 and the adsorbed H atom; and ΔS is the difference in entropy.

CRediT authorship contribution statement

H. Zhang carried out the synthesis and characterizations and collaborated on writing the manuscript. **J. Yin** conducted the DFT calculations. **T. W. B. Lo** conceived the project, directed the study, and wrote the manuscript. **Y. Wang** guided the eCO_2RR measurements. **Q. Lei** and **Y. Wang** collaborated on writing the manuscript. **C. Tang** contributed to the operando XRD reactor cell design. All authors discussed the results and contributed to the production of the manuscript.

Declaration of Competing Interest

There are no conflicts to declare.

Acknowledgements

This work was financially supported by the Department of Science and Technology of Guangdong Province (2021A1515010218), the National Natural Science Foundation of China (22172136), the Hong Kong Research Grants Council (15301521 and 15300819), PolyU start-up SHS fund (BDC3).

References

[1] Y. Xie, P. Ou, X. Wang, Z. Xu, Y.C. Li, Z. Wang, J.E. Huang, J. Wicks, C. McCallum, N. Wang, Y. Wang, T. Chen, B.T.W. Lo, D. Sinton, J.C. Yu, Y. Wang, E.H. Sargent, High carbon utilization in CO2 reduction to multi-carbon products in acidic media, Nat. Catal. 5 (2022) 564–570. https://doi.org/10.1038/s41929-022-00788-1.

[2] T.T. Zhuang, Z.Q. Liang, A. Seifitokaldani, Y. Li, P. de Luna, T. Burdyny, F. Che, F. Meng, Y. Min, R. Quintero-Bermudez, C.T. Dinh, Y. Pang, M. Zhong, B. Zhang, J. Li, P.N. Chen, X.L. Zheng, H. Liang, W.N. Ge, B.J. Ye, D. Sinton, S.H. Yu, E.H. Sargent, Steering post-C-C coupling selectivity enables high efficiency electroreduction of carbon dioxide to multi-carbon alcohols, Nat. Catal. 1 (2018) 421–428. https://doi.org/10.1038/s41929-018-0084-7.

[3] D.H. Nam, P. de Luna, A. Rosas-Hernández, A. Thevenon, F. Li, T. Agapie, J.C. Peters, O. Shekhah, M. Eddaoudi, E.H. Sargent, Molecular enhancement of heterogeneous CO2 reduction, Nat. Mater. 19 (2020) 266–276. https://doi.org/10.1038/s41563-020-0610-2.

[4] F.P. García de Arquer, C.T. Dinh, A. Ozden, J. Wicks, C. McCallum, A.R. Kirmani, D.H. Nam, C. Gabardo, A. Seifitokaldani, X. Wang, Y.C. Li, F. Li, J. Edwards, L.J. Richter, S.J. Thorpe, D. Sinton, E.H. Sargent, CO2 electrolysis to multicarbon products at activities greater than 1 A cm^{-2}, Science. 367 (2020) 661–666. https://doi.org/10.1126/science.aay4217.

[5] C. Zhan, F. Dattila, C. Rettenmaier, A. Bergmann, S. Kühl, R. García-Muelas, N. López, B. Roldan Cuenya, Revealing the CO Coverage-Driven C-C Coupling Mechanism for Electrochemical CO2 Reduction on Cu2O Nanocubesvia OperandoRaman Spectroscopy, ACS Catal. 11 (2021) 7694–7701. https://doi.org/10.1021/acscatal.1c01478.

[6] C.T. Dinh, T. Burdyny, G. Kibria, A. Seifitokaldani, C.M. Gabardo, F. Pelayo García De Arquer, A. Kiani, J.P. Edwards, P. de Luna, O.S. Bushuyev, C. Zou, R. Quintero-Bermudez, Y. Pang, D. Sinton, E.H. Sargent, CO2 electroreduction to ethylene via hydroxide-mediated copper catalysis at an abrupt interface, Science. 360 (2018) 783–787. https://doi.org/10.1126/science.aas9100.

[7] A. Vasileff, C. Xu, Y. Jiao, Y. Zheng, S.Z. Qiao, Surface and Interface Engineering in Copper-Based Bimetallic Materials for Selective CO2 Electroreduction, Chem. 4 (2018) 1809–1831. https://doi.org/10.1016/j.chempr.2018.05.001.

[8] A. Herzog, A. Bergmann, H.S. Jeon, J. Timoshenko, S. Kühl, C. Rettenmaier, M. Lopez Luna, F.T. Haase, B. Roldan Cuenya, Operando Investigation of Ag-Decorated Cu2O Nanocube Catalysts with Enhanced CO2 Electroreduction toward Liquid Products, Angew. Chem. Int. Ed. 60 (2021) 7426–7435. https://doi.org/10.1002/anie.202017070.

[9] L. Xiong, X. Zhang, L. Chen, Z. Deng, S. Han, Y. Chen, J. Zhong, H. Sun, Y. Lian, B. Yang, X. Yuan, H. Yu, Y. Liu, X. Yang, J. Guo, M.H. Rümmeli, Y. Jiao, Y. Peng, Geometric Modulation of Local CO Flux in Ag@Cu2O Nanoreactors for Steering the CO2RR Pathway toward High-Efficacy Methane Production, Adv. Mater. 33 (2021) 2101741. https://doi.org/10.1002/adma.202101741.

[10] Y. Jiang, X. Wang, D. Duan, C. He, J. Ma, W. Zhang, H. Liu, R. Long, Z. Li, T. Kong, X.J. Loh, L. Song, E. Ye, Y. Xiong, Structural Reconstruction of Cu2O Superparticles toward Electrocatalytic CO2 Reduction with High C2+ Products Selectivity, Adv. Sci. 9 (2022) 2105292. https://doi.org/10.1002/advs.202105292.

[11] Z. Zhang, Y. Xie, Y. Wang, What matters in the emerging application of CO2 electrolysis, Curr. Opin. Electrochem. 34 (2022) 101012. https://doi.org/10.1016/j.coelec.2022.101012.

[12] Y. Wang, B.J. Park, V.K. Paidi, R. Huang, Y. Lee, K.J. Noh, K.S. Lee, J.W. Han, Precisely Constructing Orbital Coupling-Modulated Dual-Atom Fe Pair Sites for Synergistic CO2 Electroreduction, ACS Energy Lett. 7 (2022) 640–649. https://doi.org/10.1021/acsenergylett.1c02446.

[13] M. Luo, Z. Wang, Y.C. Li, J. Li, F. Li, Y. Lum, D.H. Nam, B. Chen, J. Wicks, A. Xu, T. Zhuang, W.R. Leow, X. Wang, C.T. Dinh, Y. Wang, Y. Wang, D. Sinton, E.H. Sargent, Hydroxide promotes carbon dioxide electroreduction to ethanol on copper via tuning of adsorbed hydrogen, Nat. Commun. 10 (2019) 5814. https://doi.org/10.1038/s41467-019-13833-8.

[14] B. Liu, X. Yao, Z. Zhang, C. Li, J. Zhang, P. Wang, J. Zhao, Y. Guo, J. Sun, C. Zhao, Synthesis of Cu2O Nanostructures with Tunable Crystal Facets for Electrochemical CO2 Reduction to Alcohols, ACS Appl. Mater. Interfaces. 13 (2021) 39165–39177. https://doi.org/10.1021/acsami.1c03850.

[15] U.O. Nwabara, M.P. de Heer, E.R. Cofell, S. Verma, E. Negro, P.J.A. Kenis, Towards accelerated durability testing protocols for CO2 electrolysis, J. Mater. Chem. A Mater. 8 (2020) 22557–22571. https://doi.org/10.1039/D0TA08695A.

[16] C.W. Li, M.W. Kanan, CO2 reduction at low overpotential on Cu electrodes resulting from the reduction of thick Cu2O films, J. Am. Chem. Soc. 134 (2012) 7231–7234. https://doi.org/10.1021/ja3010978.

[17] Y. Gao, Q. Wu, X. Liang, Z. Wang, Z. Zheng, P. Wang, Y. Liu, Y. Dai, M.H. Whangbo, B. Huang, Cu2O Nanoparticles with Both {100} and {111} Facets for Enhancing the Selectivity and Activity of CO2 Electroreduction to Ethylene, Adv. Sci. 7 (2020). 1902820 https://doi.org/10.1002/advs.201902820.

[18] L. Mandal, K.R. Yang, M.R. Motapothula, D. Ren, P. Lobaccaro, A. Patra, M. Sherburne, V.S. Batista, B.S. Yeo, J.W. Ager, J. Martin, T. Venkatesan, Investigating the Role of Copper Oxide in Electrochemical CO2 Reduction in Real Time, ACS Appl. Mater. Interfaces. 10 (2018) 8574–8584. https://doi.org/10.1021/acsami.7b15418.

[19] H. Mistry, A.S. Varela, C.S. Bonifacio, I. Zegkinoglou, I. Sinev, Y.W. Choi, K. Kisslinger, E.A. Stach, J.C. Yang, P. Strasser, B.R. Cuenya, Highly selective plasma-activated copper catalysts for carbon dioxide reduction to ethylene, Nat. Commun. 7 (2016) 12123. https://doi.org/10.1038/ncomms12123.

[20] M. Favaro, H. Xiao, T. Cheng, W.A. Goddard, E.J. Crumlin, Subsurface oxide plays a critical role in CO2 activation by Cu(111) surfaces to form chemisorbed CO2, the first step in reduction of CO2, PNAS. 114 (2017) 6706–6711. https://doi.org/10.1073/pnas.1701405114.

[21] F. Cavalca, R. Ferragut, S. Aghion, A. Eilert, O. Diaz-Morales, C. Liu, A.L. Koh, T.W. Hansen, L.G.M. Pettersson, A. Nilsson, Nature and distribution of stable subsurface oxygen in copper electrodes during electrochemical CO2 reduction, J. Phys. Chem. C 121 (2017) 25003–25009. https://doi.org/10.1021/acs.jpcc.7b08278.

[22] L. Zhai, T.W. Benedict Lo, Z.-L. Xu, J. Potter, J. Mo, X. Guo, C.C. Tang, S.C. Edman Tsang, S.P. Lau, In Situ Phase Transformation on Nickel-Based Selenides for Enhanced Hydrogen Evolution Reaction in Alkaline Medium, ACS Energy Lett. 5 (2020) 2483–2491. https://doi.org/10.1021/acsenergylett.0c01385.

[23] Y. Yang, S. Louisia, S. Yu, J. Jin, I. Roh, C. Chen, M. V. Fonseca Guzman, J. Feijóo, P.C. Chen, H. Wang, C.J. Pollock, X. Huang, Y.T. Shao, C. Wang, D.A. Muller, H.D. Abruña, P. Yang, Operando studies reveal active Cu nanograins for CO2 electroreduction, Nature. 614 (2023) 262–269. https://doi.org/10.1038/s41586-022-05540-0.

[24] J.J. Masana, B. Peng, Z. Shuai, M. Qiu, Y. Yu, Influence of halide ions on the electrochemical reduction of carbon dioxide over a copper surface, J. Mater. Chem. A. 10 (2022) 1086–1104. https://doi.org/10.1039/d1ta09125e.

[25] S.C. Lin, C.C. Chang, S.Y. Chiu, H.T. Pai, T.Y. Liao, C.S. Hsu, W.H. Chiang, M.K. Tsai, H.M. Chen, Operando time-resolved X-ray absorption spectroscopy reveals the chemical nature enabling highly selective CO2 reduction, Nat. Commun. 11 (2020). 3525. https://doi.org/10.1038/s41467-020-17231-3.

[26] J. Pellessier, Y. Gang, Y. Li, A Sustainable Synthesis of Nickel-Nitrogen-Carbon Catalysts for Efficient Electrochemical CO2 Reduction to CO, ES Mater. Manuf. 13 (2021) 66–75. https://doi.org/10.30919/esmm5f447.

[27] Y. Wang, S. Zhao, M. Li, W. Li, Y. Zhao, J. Qi, X. Cui, Graphene quantum dots decorated graphene as an enhanced sensing platform for sensitive and selective detection of copper(II), J. Electroanal. Chem. 797 (2017) 113–120. https://doi.org/10.1016/j.jelechem.2017.05.031.

[28] H. Luo, B. Li, J.G. Ma, P. Cheng, Surface Modification of Nano-Cu2O for Controlling CO2 Electrochemical Reduction to Ethylene and Syngas, Angew. Chem. Int. Ed. 61 (2022) e202116736. https://doi.org/10.1002/anie.202116736.

[29] L.R.L. Ting, O. Piqué, S.Y. Lim, M. Tanhaei, F. Calle-Vallejo, B.S. Yeo, Enhancing CO2 Electroreduction to Ethanol on Copper-Silver Composites by Opening an Alternative Catalytic Pathway, ACS Catal. 10 (2020) 4059–4069. https://doi.org/10.1021/acscatal.9b05319.

[30] X. Wang, J.F. de Araújo, W. Ju, A. Bagger, H. Schmies, S. Kühl, J. Rossmeisl, P. Strasser, Mechanistic reaction pathways of enhanced ethylene yields during electroreduction of CO2–CO co-feeds on Cu and Cu-tandem electrocatalysts, Nat. Nanotechnol. 14 (2019) 1063–1070. https://doi.org/10.1038/s41565-019-0551-6.

[31] G. Liu, M. Lee, S. Kwon, G. Zeng, J. Eichhorn, A.K. Buckley, F.D. Toste, W.A. Goddard, F.M. Toma, CO2 reduction on pure Cu produces only H2 after subsurface O is depleted: Theory and experiment, PNAS 118 (2021) e2012649118. https://doi.org/10.1073/pnas.2012649118.

[32] Q. Lei, L. Huang, J. Yin, B. Davaasuren, Y. Yuan, X. Dong, Z.P. Wu, X. Wang, K.X. Yao, X. Lu, Y. Han, Structural evolution and strain generation of derived-Cu catalysts during CO2 electroreduction, Nat. Commun. 13 (2022) 4857. https://doi.org/10.1038/s41467-022-32601-9.

[33] B.T.W. Lo, L. Ye, J. Qu, J. Sun, J. Zheng, D. Kong, C.A. Murray, C.C. Tang, S.C.E. Tsang, Elucidation of Adsorbate Structures and Interactions on Brønsted Acid Sites in H-ZSM-5 by Synchrotron X-ray Powder Diffraction, Angew. Chem. Int. Ed. 55 (2016) 5981–5984. https://doi.org/10.1002/anie.201600487.

[34] L.N. Wu, Z.Y. Tian, W. Qin, DFT Study on CO Catalytic Oxidation Mechanism on the Defective Cu2O(111) Surface, Journal of Physical Chemistry C. 122 (2018) 16733–16740. https://doi.org/10.1021/ACS.JPCC.8B03471/

[35] J. Song, C. Yang, H. Hu, X. Dai, C. Wang, H. Zhang, Penetration depth at various Raman excitation wavelengths and stress model for Raman spectrum in biaxially-strained Si, Sci. China: Phys. Mech. Astron 56 (2013) 2065–2070. https://doi.org/10.1007/S11433-013-5205-3.

[36] J. Wang, H. Tan, Y. Zhu, H. Chu, H.M. Chen, Linking the Dynamic Chemical State of Catalysts with the Product Profile of Electrocatalytic CO2 Reduction, Angew. Chem. Int. Ed. 133 (2021) 17394–17407. https://doi.org/10.1002/ange.202017181.

[37] C. Ravichandiran, A. Sakthivelu, K. Deva Arun Kumar, R. Davidprabu, S. Valanarasu, A. Kathalingam, V. Ganesh, M. Shkir, H. Algarni, S. AlFaify, Influence of rare earth material (Sm3+) doping on the properties of electrodeposited Cu2O films for optoelectronics, J. Mater. Sci.: Mater. Electron. 30 (2019) 2530–2537. https://doi.org/10.1007/S10854-018-0527-6/

[38] L. Jin, A. Seifitokaldani, In situ spectroscopic methods for electrocatalytic CO2 reduction, Catalysts 10 (2020) 481. https://doi.org/10.3390/catal10050481.

[39] C. Chen, X. Yan, Y. Wu, S. Liu, X. Sun, Q. Zhu, R. Feng, T. Wu, Q. Qian, H. Liu, L. Zheng, J. Zhang, B. Han, Thein situstudy of surface species and structures of oxide-derived copper catalysts for electrochemical CO2 reduction, Chem. Sci. 12 (2021) 5938–5943. https://doi.org/10.1039/d1sc00042j.

[40] R. Zhang, H. Wang, S. Tang, C. Liu, F. Dong, H. Yue, B. Liang, Photocatalytic Oxidative Dehydrogenation of Ethane Using CO2 as a Soft Oxidant over Pd/TiO2 Catalysts to C2H4 and Syngas, ACS Catal. 8 (2018) 9280–9286. https://doi.org/10.1021/acscatal.8b02441.

[41] K. Dong Yang, C. Woo Lee, K. Jin, S. Won Im, K. Tae Nam, Current Status and Bioinspired Perspective of Electrochemical Conversion of CO2 to a Long-Chain Hydrocarbon, J. Phys. Chem. Lett. 8 (2017) 538–545. https://doi.org/10.1021/acs.jpclett.6b02748.

[42] G. Jia, M. Sun, Y. Wang, Y. Shi, L. Zhang, X. Cui, B. Huang, J.C. Yu, Asymmetric Coupled Dual-Atom Sites for Selective Photoreduction of Carbon Dioxide to Acetic Acid, Adv. Funct. Mater. 32 (2022) 2206817. https://doi.org/10.1002/adfm.202206817.

[43] Z.Z. Wu, X.L. Zhang, Z.Z. Niu, F.Y. Gao, P.P. Yang, L.P. Chi, L. Shi, W. Wei, R. Liu, Z. Chen, S. Hu, X. Zheng, M.R. Gao, Identification of Cu(100)/Cu(111) Interfaces as

Superior Active Sites for CO Dimerization during CO2 Electroreduction, J. Am. Chem. Soc. 144 (2022) 259–269. https://doi.org/10.1021/jacs.1c09508.

[44] J. Huang, N. Hörmann, E. Oveisi, A. Loiudice, G.L. de Gregorio, O. Andreussi, N. Marzari, R. Buonsanti, Potential-induced nanoclustering of metallic catalysts during electrochemical CO2 reduction, Nat. Commun. 9 (2018) 3117. https://doi.org/10.1038/s41467-018-05544-3.

[45] H. Xiao, W.A. Goddard, T. Cheng, Y. Liu, Cu metal embedded in oxidized matrix catalyst to promote CO2 activation and CO dimerization for electrochemical reduction of CO2, PNAS. 114 (2017) 6685–6688. https://doi.org/10.1073/pnas.1702405114.

[46] A. Verdaguer-Casadevall, C.W. Li, T.P. Johansson, S.B. Scott, J.T. McKeown, M. Kumar, I.E.L. Stephens, M.W. Kanan, I. Chorkendorff, Probing the Active Surface Sites for CO Reduction on Oxide-Derived Copper Electrocatalysts, J. Am. Chem. Soc. 137 (2015) 9808–9811. https://doi.org/10.1021/jacs.5b06227.

[47] S. Jiao, X. Fu, H. Huang, Descriptors for the Evaluation of Electrocatalytic Reactions: d-Band Theory and Beyond, Adv. Funct. Mater. 32 (2022) 2107651. https://doi.org/10.1002/adfm.202107651.

[48] Q. Hu, K. Gao, X. Wang, H. Zheng, J. Cao, L. Mi, Q. Huo, H. Yang, J. Liu, C. He, Subnanometric Ru clusters with upshifted D band center improve performance for alkaline hydrogen evolution reaction, Nat. Commun. 13 (2022) 3958. https://doi.org/10.1038/s41467-022-31660-2.

[49] A.J. Garza, A.T. Bell, M. Head-Gordon, Is Subsurface Oxygen Necessary for the Electrochemical Reduction of CO2 on Copper?, Journal of Physical Chemistry Letters. 9 (2018) 601–606. https://doi.org/10.1021/acs.jpclett.7b03180.

[50] C. Liu, M.P. Lourenço, S. Hedström, F. Cavalca, O. Diaz-Morales, H.A. Duarte, A. Nilsson, L.G.M. Pettersson, Stability and effects of subsurface oxygen in oxide-derived Cu catalyst for CO2 reduction, Journal of Physical Chemistry C. 121 (2017) 25010–25017. https://doi.org/10.1021/ACS.JPCC.7B08269/

[51] W. Fu, Z. Liu, T. Wang, J. Liang, S. Duan, L. Xie, J. Han, Q. Li, Promoting C2+Production from Electrochemical CO2Reduction on Shape-Controlled Cuprous Oxide Nanocrystals with High-Index Facets, ACS Sustain Chem. Eng. 8 (2020) 15223–15229. https://doi.org/10.1021/acssuschemeng.0c04873.

[52] Z. Zhao, X. Wang, J. Si, C. Yue, C. Xia, F. Li, Truncated concave octahedral Cu2O nanocrystals with {Hkk} high-index facets for enhanced activity and stability in heterogeneous catalytic az-ide-alkyne cycloaddition, Green Chem. 20 (2018) 832–837. https://doi.org/10.1039/c7gc03020g.

[53] Y. Tan, X. Xue, Q. Peng, H. Zhao, T. Wang, Y. Li, Controllable fabrication and electrical performance of single crystalline Cu2O nanowires with high aspect ratios, Nano Lett. 7 (2007) 3723–3728. https://doi.org/10.1021/nl0721259.

[54] B. Ravel, M. Newville, ATHENA, ARTEMIS, HEPHAESTUS: data analysis for X-ray absorption spectroscopy using IFEFFIT, J Synchrotron Radiat. 12 (2005) 537–541. https://doi.org/10.1107/S0909049505012719.

[55] H. Funke, A.C. Scheinost, M. Chukalina, Wavelet analysis of extended x-ray absorption fine structure data, M. Phys. Rev. B. 71 (2005) 094110 https://doi.org/10.1103/PhysRevB.71.094110.

[56] P. Thompson, D. E. Cox and J. B. Hastings, Rietveld Refinement of Debye-Scherrer Synchrotron X-ray Data from Al2O3, J. Appl. Cryst. 20 (1987) 79–83. https://doi.org/10.1107/S0021889887087090

[57] G. Kresse, J. Furthmüller, Efficient iterative schemes for ab initio total-energy calculations using a plane-wave basis set, J. Phys. Rev. B 54 (1996) 11169–11186. https://doi.org/10.1103/PhysRevB.54.11169.

[58] G. Kresse, J. Hafner, Ab initio molecular dynamics for open-shell transition metals, J. Ab. Phys. Rev. B 48 (1993) 13115–13118. https://doi.org/10.1103/PhysRevB.48.13115.